


## Secondary particle predictions in quasifree proton scattering reactions in the 100–250 MeV energy range

E. Cupertino Gomes <sup>\*</sup>, U. B. Rodríguez , and M. Gonçalves 

*Instituto de Radioproteção e Dosimetria, Avenida Salvador Allende, 3773, 22783-127 Rio de Janeiro, Rio de Janeiro, Brazil*

A. R. C. Pinheiro , B. M. Santos, and C. R. R. Souza

*Universidade Federal do Acre, BR 364 Km 04, 69920-900 Rio Branco, Acre, Brazil*

L. R. Hirsch

*Universidade Tecnológica Federal do Paraná, Avenida Sete de Setembro, 80230-900 Curitiba, Paraná, Brazil*

S. B. Duarte 

*Centro Brasileiro de Pesquisas Físicas, Rua Doutor Xavier Sigaud 150, 22290-180 Rio de Janeiro, Rio de Janeiro, Brazil*



(Received 24 October 2022; accepted 17 January 2023; published 21 February 2023)

Results for observables related to the secondary particle production process in proton-nucleus spallation reactions at low beam incident energy (100–250 MeV) are shown. The energy and angular distributions of the residual nucleus are determined in the context of our multicollisional Monte Carlo intranuclear cascade model. The mechanism of proton-nucleus reactions is conventionally described as a sequence of two stages: the rapid intranuclear cascade phase and the slow particle evaporation step. In this work we focus on the rapid phase considering the nucleon effective mass as an effect of the many-body nuclear interactions and the intranuclear mean field. This procedure represents a more realistic scenario to obtain the particles' multiplicity generated in spallation reactions with light-mass target nuclei in a low-energy range. We focused our attention on target nuclei of macro elements, such as carbon, oxygen, phosphorus, sulfur, sodium, potassium, chlorine, and calcium, and trace elements such as iron, copper, zinc, bromine and selenium, which are the most frequent compounds of the organic material. The choice of these target nuclei is due to our expectancy that our results can work as a preliminary insight for further theoretical approaches, specially taking into account nuclear effects due to the interaction of the particles of the beam with the organic tissue.

DOI: [10.1103/PhysRevC.107.024613](https://doi.org/10.1103/PhysRevC.107.024613)

### I. INTRODUCTION

In the present work, we focus on the proton-nucleus spallation reactions [1,2] to discuss intranuclear multicollisional processes. The nuclear spallation reaction induced by protons has been well described as a two-step process [3]. In the first stage, the high-energy incident proton interacts with the target nucleus, transferring part of or the whole beam energy to the nuclear system by multicollisional processes in a rapid phase, namely, the cascade phase [4–8]. During the intranuclear dynamics, nucleons can be ejected from the nuclear environment and these escaping particles carry part of the energy initially deposited in the target nucleus. As a result the remaining energy of the system is redistributed in a pre-equilibrium phase, leading the residual nucleus to a final thermal equilibrium state [9]. The pion formation process [10,11] may also play an important role in the cooling mechanism of the target nucleus, since part of the beam energy may be converted internally in

pion mass and rendered to the nuclear environment only in the final stage of the cascade phase.

Although the evaporation phase could be important for the determination of low-energy emitted particles, the main goal of the present calculation is to investigate the nuclear effects on the proton interaction with the atomic nucleus in terms of an effective baryonic mass. We anticipate that only a small number of energetic particles of few tens of MeV are emitted in the cascade phase (energy value  $\geq 20$  MeV). However, they are quite important to the determination of the final spectra and angular distribution of high-energy emitted particles, of practical interest for other fields of investigation such as particle therapy and waste renewal by accelerators [12,13].

In previous works [4,5,14], we demonstrated that the characteristics of the residual cascade nuclei (atomic number, mass number, and excitation energy) are remarkably sensitive to the value attributed to the nucleon effective mass. A fundamental aspect of nucleons' behavior in the nuclear environment is the change in their kinematic properties due to the nuclear *in-medium* interactions. The concept of baryon effective mass is introduced to determine the propagation of nucleons inside the nuclear environment. This concept comes

<sup>\*</sup>Present address: Universidade Federal do Norte do Tocantins, Avenida Paraguaí, s/n°, 77824-838, Araguaína, Tocantins, Brazil.

from a mean-field approximation and other more fundamental approaches to describe nuclear matter and finite nucleus structure [15]. In this context, we have introduced a nucleon effective mass in the ground state to mimic the effects of the nuclear mean field. During  $p - A$  reactions, the effective mass is redefined in order to strictly preserve the energy-momentum conservation principle. The inclusion of mean-field properties in the intranuclear reactions dynamics has already been performed in earlier works by Boudard *et al.* [16], Aoust and Cugnon [17], Jaminon and Mahaux [18,19], David [20], and Filges *et al.* [21], among others. The effective mass prescription described in the present work is an alternative for these earlier calculations in a manner that nuclear effects can be properly controlled in the cascade mechanism as an initial free parameter that changes during the intranuclear dynamics.

The analysis of the behavior of particle production in low-energy proton-nucleus spallation reactions faced with changes in nucleon effective mass, energy beam, and target nucleus mass is performed throughout the present work. We focus our attention on target nuclei which mainly compose organic tissue, i.e., the majority elements (C, N, O, Na, P, S, Cl, K, and Ca) and the trace elements (Fe, Cu, Zn, and Se), as well as prosthesis elements such as W and Pt. This information can be very important to medical applications in the determination of doses in proton-therapy treatment plans as well as to the physics of particle driven accelerators (ADS) [14,22–24], where Pb is the main target nucleus. We leave the dose determination for other authors who deal with particle transport calculations such as GEANT or MCNP, among others, and we expect our results will help these investigations toward a more precise determination of the absorbed dose from secondary particles emitted during the interaction with the particles of a beam with organic tissue [25,26].

The paper is organized as follows. In Sec. II, we give brief lines and some relevant details of the multicollisional Monte Carlo (MCMC) model, focused only on the cascade phase of the reaction. The energy and angular distribution of the secondary particles are presented and discussed in Sec. III. The conclusions and final remarks are presented in Sec. IV.

## II. MCMC: MULTICOLLISIONAL MONTE CARLO MODEL

### A. Particle interactions and transport

Proton-nucleus interactions in the energy range of 100–250 MeV can be described by a series of nucleon-nucleon binary interactions. The pion production takes place mostly near the direct pion production threshold. The collisional processes taken into account in the model are listed in Table I.

After the interaction of the beam with target nucleus takes place, the so called primary interaction, the calculation scheme follows the time evolution of sequential binary collisions between particles of the overall system [3,27–29], and some quantities of interest, such as the number of ejected particles, their kinetic energy values and their angular distributions, are determined. More details about the numerical code and model parametrization can be found in Refs. [5,28,30]. Although there are a few numerical codes and models which

TABLE I. Collisional processes considered in the MCMC description.

Interaction	Description
$B_1 B_2 \rightarrow B_1 B_2$	Baryon-baryon elastic collision
$NN \rightarrow N\Delta$	$\Delta$ -resonance formation
$N\Delta \rightarrow NN$	$\Delta$ -resonance recombination
$NN \rightarrow NN^*$	$N^*$ -resonance formation
$NN^* \rightarrow NN$	$N^*$ -resonance recombination
$\Delta \rightarrow N\pi$	Pion production
$N^* \rightarrow N\pi$	
$N\pi \rightarrow \Delta$	Pion absorption
$N\pi \rightarrow N^*$	

perform the energy transport through matter, such as GEANT [31], FLUKA [32], and MCNP [33], we emphasize that these models do not deal with mean-field effects, disregarding their importance on the mechanism of secondary particle production.

The present calculation, performed with the MCMC code, does not consider particle or energy transport in material, since we focus our attention on the most significant ingredients of the beam-nucleus interaction, bringing light to intranuclear phenomena and to effects on the particle production and differential cross sections. The task of propagating the secondary particles in tissue should be performed in the context of one of the abovementioned numerical algorithms on a subsequent phase of the dynamics.

In our semiclassical prediction, the Pauli exclusion principle has been prohibiting collisions for which nucleons' final states are within a Fermi sphere of radius around 270 MeV/c. Differently from conventional cascade calculations, we contemplate the many-body evolution of all nucleons in the system, considering all possible baryon-baryon and meson-baryon interactions. Because we are dealing with the complete time evolution of a many-particle system, this approach allows us to treat the rapid phase and also the transient pre-equilibrium phase within a single theoretical framework.

The MCMC description also traps nucleons within a potential well where surface reflection and refraction processes can take place. We evaluate dynamically the population of emitted particles in the cascade phase, which ends when the following conditions are simultaneously satisfied:

- (i) all elastic collisions are Pauli blocked,
- (ii) no particle has enough energy to escape from the nucleus, and
- (iii) all resonances have decayed.

When all these conditions are simultaneously satisfied, we consider that a hot residual nucleus is formed and its excitation energy value is obtained.

### B. Effective mass in intranuclear cascade phase

The cascade time evolution and the kinematics of collisional processes involving bound baryons are treated in terms of an effective mass,  $m^*$ , for these particles. The initial mass

TABLE II. Nuclear spherical potential well depth,  $V_0$ , determined for different initial values of the effective mass  $m_0^*$  in units of the nucleon free mass,  $m_0$ .

$m_0^* (m_0)$	$V_0$ (MeV)
0.60	62.13
0.70	54.95
0.80	49.41
0.90	45.01
1.00	41.44

value,  $m_0^*$ , for each nucleon in the nucleus ground state can be estimated from mean-field theories for the nuclear matter in equilibrium [34]. Different microscopic theories have given insights for these values in the range  $0.6m_0$  to  $1.0m_0$  ( $m_0$  is the free nucleon mass); then we introduced the  $m_0^*$  value as a free parameter to discuss the effect of this quantity on particle emission distributions.

Due to the inclusion of the initial effective mass value ( $m_0^*$ ) on the nucleon dispersion relation, the possibility of particles escaping from the nuclear system in its ground state introduces a dependence of the potential well depth  $V_0$  of the target nucleus on this  $m_0^*$ . In Table II, we show the results for the depth of the spherical well employed to restrict particles to the nuclear volume. This procedure ensures that there is no spurious escape of particles from the nucleus in the dynamical simulation.

During the time evolution of the effective mass of bound nucleons, the conservation of the total momentum and energy of the system is imposed for all baryonic processes. Also, in the cascade phase when the  $i$  nucleon leaves the nuclear environment its effective mass must be replaced by the free mass value, i.e.,

$$m_i^* \rightarrow m_0.$$

In order to strictly conserve the total energy and momentum of the system, we have imposed that all remaining  $j$ -bound-baryons should have their effective mass recalculated as  $\forall_{j \neq i} (m_j^* \rightarrow \alpha m_j^*)$ . With this prescription, bound particles' effective mass evolves by a multiplicative factor  $\alpha$  whenever a baryon leaves the system. This multiplicative factor is given in terms of the energy-momentum conservation for all particles in the nuclear system, being explicitly determined as

$$\alpha = \frac{E'E + [(E'E)^2 - (E'^2 - p_i^2)(E^2 - m_0^2)]^{1/2}}{(E'^2 - p_i^2)}, \quad (1)$$

where  $E$  is the total energy of all baryons before the nucleon escape and  $E'$  is the total energy of the remaining particles.

The MCMC model has been confronted in the last decades against experimental results in order to validate obtained results. In the next section, we validate the model against some experimental results.

### C. Model validation

For the sake of validation of the current model we compare the calculations with the experimental cross section of

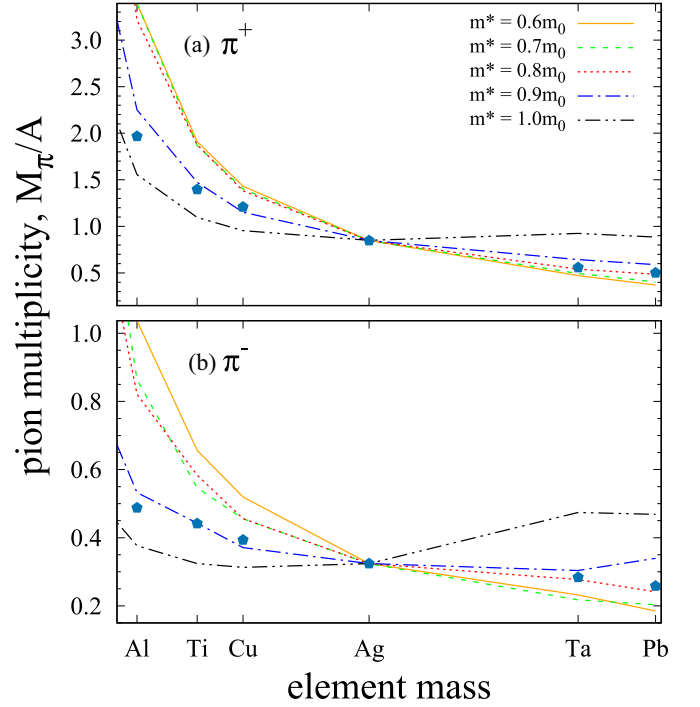


FIG. 1. Pion multiplicity as a function of target nucleus mass for different  $m_0^*$  values in the intranuclear cascade phase compared with the experimental production of charged pions by 730-MeV protons (taken from Cochran *et al.* [35]).

produced pions by 730-MeV protons, measured by Cochran *et al.* [35]. We chose pion production results due to the high emitted particle yield because it could provide a more precise determination of the initial effective mass value for nucleons ( $m_0^*$ ). In Fig. 1(a) we display the pion multiplicity calculated with MCMC for five different values of  $m_0^*$  ( $0.6m_0$ ,  $0.7m_0$ ,  $0.8m_0$ ,  $0.9m_0$ , and  $1.0m_0$ ) and we compare the results with data for  $\pi^-$  and  $\pi^+$  production. The curve that presents the smallest  $\sigma$  value (not shown) is that for  $m_0^* = 0.9m_0$  and we use this value as a fixed parameter for all other calculations [35].

We decided to center our results in the  $p$ -Ag reaction, which by its turn, is roughly the center of the target nucleus mass number range considered in the present work. Results are displayed in arbitrary units because our goal is to infer the best  $m_0^*$  value from the experimental cross section, disregarding specific experiment characteristics such as foil thickness, particle flux or current, impact parameter, and so forth.

Besides pion production, secondary proton and neutron emissions can also work as delimiters of the model. In Fig. 2, we contrast results of the MCMC model with experimental data for  $^{12}\text{C}(p, p')$  reactions at 200-MeV incident energy. The residual energy  $\omega_e$  is defined in Ref. [36] and, as one can see, there is a reasonable coincidence between theoretical and experimental results for scattered protons after the interaction of the proton beam with the target nucleus.

A similarly good agreement is observed when MCMC results are compared to the experimental correlated  $(n, p)$  pair observed by Carman in the same experiment. Figure 3 compares our results with data, showing a especially good

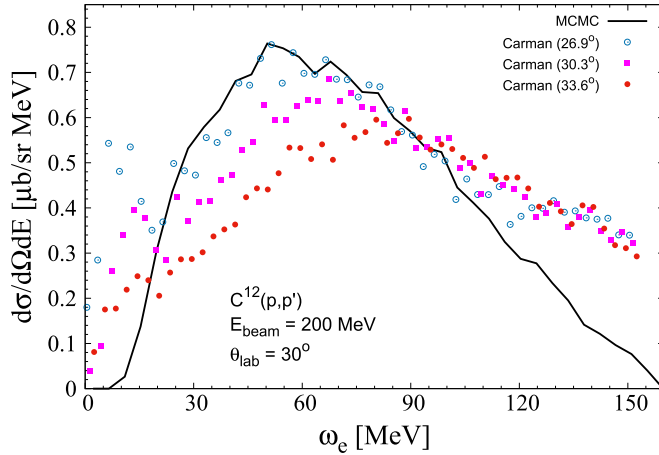


FIG. 2. Scattered protons in  $^{12}\text{C}(p, p')$  reactions at 200-MeV incident energy. The agreement with data from Carman *et al.* [36] is remarkable for the entire range of kinetic energy of the emitted nucleon.

agreement for high-energy emitted nucleons. Also, the present cascade calculation enhances low-energy particle emission due to the internal nucleon-nucleon interactions, which thermalize the nucleus faster than expected. However, because the focus of the present calculation is the high-energy particle emission, this deviation of theoretical from experimental results is considered to not affect our final results.

After the calibration of our model for the initial effective mass of the target nuclei, as well as for the depth of nuclear well and the agreement with experimental data, we follow with the presentation of our results for other proton-nuclei reactions and incident beam energies. In the next section we describe these results.

### III. RESULTS

Current results are an average over the final states of a large number of Monte Carlo samples. These final-state con-

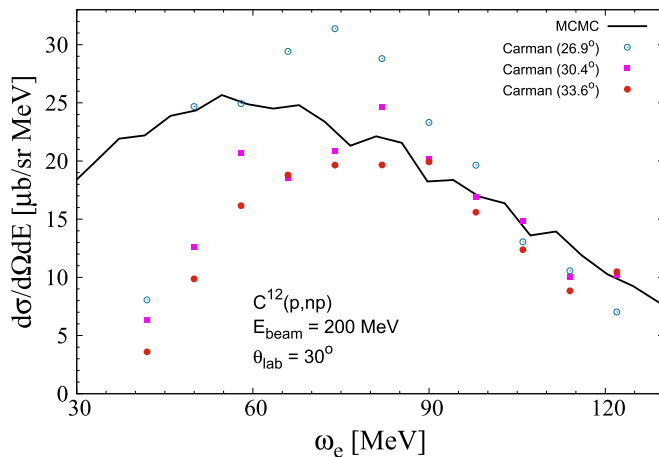


FIG. 3. Scattered correlated pair  $(n, p)$  in  $^{12}\text{C}(p, np)$  reactions at 200-MeV incident energy. The agreement with data from Carman *et al.* [36] is observed mainly for the high-energy region of the spectra.

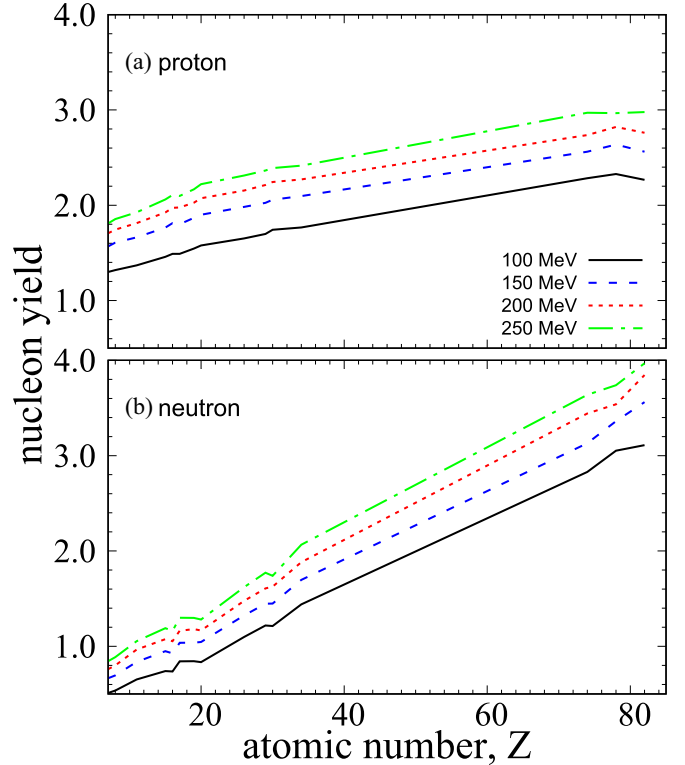


FIG. 4. Proton (a) and neutron (b) yields during the cascade phase at the initial effective mass. Solid, dashed, dotted, and dash-dotted lines stand for incident proton energies of 100, 150, 200, and 250 MeV, respectively. The horizontal axis represents the target nuclei atomic numbers of Table III. All angles labeled in the figure refer to the middle of a  $15^\circ$  window.

TABLE III. Proton and neutron yields after beam interaction with atomic nuclei. All data are presented for the incident proton energies  $E_p = 100, 150, 200,$  and  $250$  MeV.

El	100 MeV		150 MeV		200 MeV		250 MeV	
	$\langle p \rangle$	$\langle n \rangle$	$\langle p \rangle$	$\langle n \rangle$	$\langle p \rangle$	$\langle n \rangle$	$\langle p \rangle$	$\langle n \rangle$
$^{12}\text{C}$	1.274	0.475	1.540	0.627	1.670	0.719	1.764	0.798
$^{14}\text{N}$	1.299	0.510	1.568	0.664	1.706	0.760	1.809	0.843
$^{16}\text{O}$	1.319	0.535	1.607	0.695	1.744	0.799	1.854	0.886
$^{23}\text{Na}$	1.369	0.652	1.663	0.837	1.812	0.966	1.926	1.054
$^{31}\text{P}$	1.459	0.740	1.765	0.949	1.924	1.075	2.061	1.190
$^{32}\text{S}$	1.489	0.735	1.812	0.926	1.973	1.054	2.108	1.161
$^{36}\text{Cl}$	1.490	0.842	1.800	1.037	1.976	1.163	2.097	1.299
$^{39}\text{K}$	1.545	0.844	1.868	1.038	2.026	1.180	2.167	1.298
$^{40}\text{Ca}$	1.412	0.670	1.900	1.045	2.073	1.165	2.215	1.281
$^{56}\text{Fe}$	1.652	1.097	1.983	1.323	2.154	1.476	2.312	1.620
$^{64}\text{Cu}$	1.698	1.218	2.025	1.446	2.213	1.607	2.364	1.771
$^{65}\text{Zn}$	1.743	1.213	2.058	1.448	2.243	1.625	2.390	1.739
$^{79}\text{Se}$	1.767	1.439	2.096	1.697	2.271	1.882	2.416	2.065
$^{184}\text{W}$	2.283	2.829	2.562	3.130	2.737	3.442	2.970	3.638
$^{195}\text{Pt}$	2.327	3.052	2.637	3.361	2.821	3.539	2.966	3.739
$^{208}\text{Pb}$	2.500	3.200	2.800	3.500	3.000	3.700	3.200	3.900

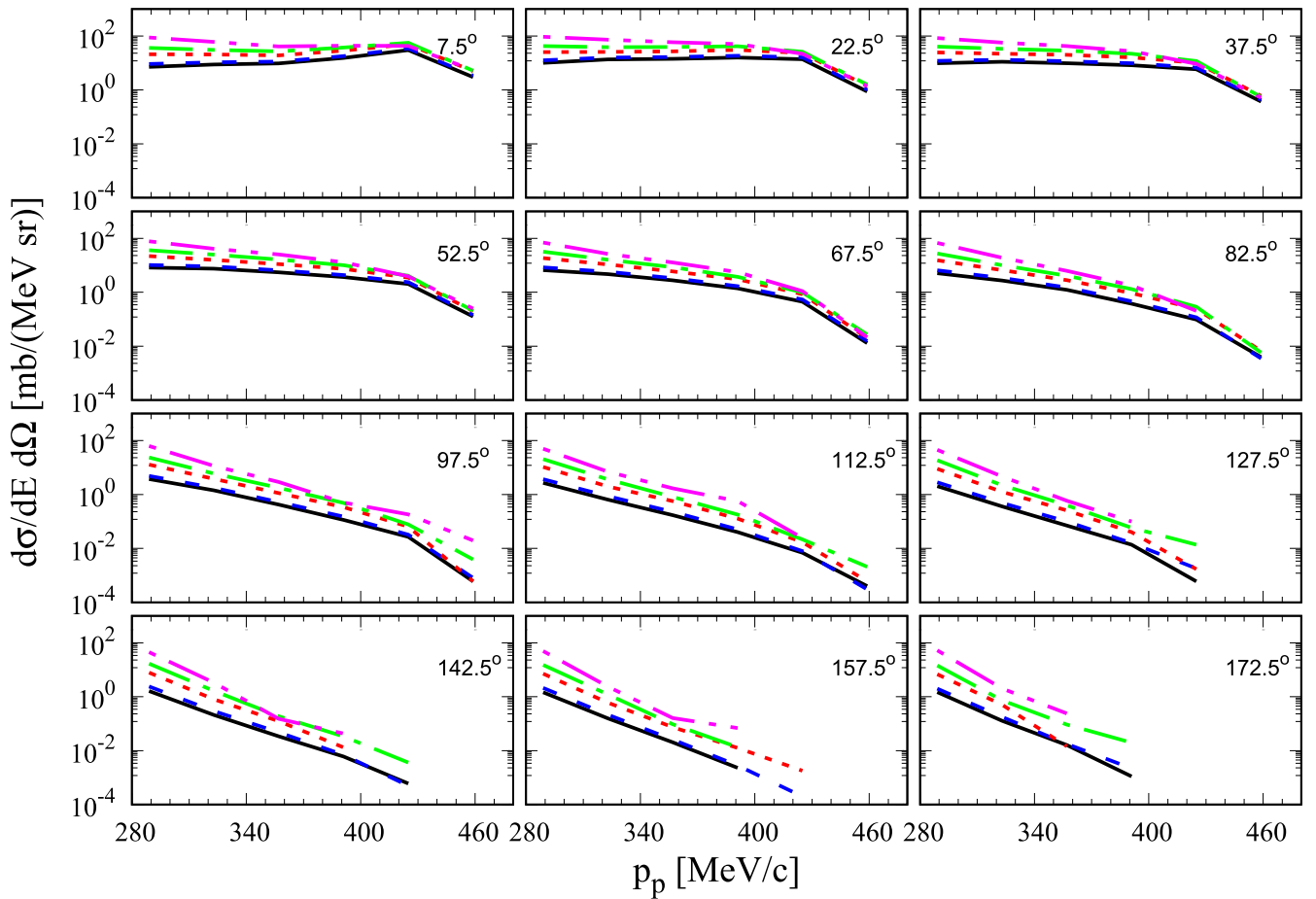


FIG. 5. Proton spectra for monoenergetic  $p - A$  reactions with 100-MeV incident energy. Panels correspond to the emitted proton detection in different  $15^\circ$  windows, varying from frontal emission ( $0 \leq \theta \leq 15$ ), transversal emission ( $75 \leq \theta \leq 90$ ), and backward emission ( $165 \leq \theta \leq 180$ ). Solid lines show results for  $p$ -C reactions, dashed lines display results for  $p$ -O reactions, dotted lines display results for  $p$ -Ca reactions, dash-dotted lines stand for  $p$ -Se, and dot-dot-dashed lines stand for  $p$ -Pb.

figurations are achieved after the computational simulation of the time evolution of the whole nuclear system in terms of a sequence of intranuclear interactions. Yield, energy, and angular distributions of produced particles are displayed only after having statistical convergence assured in the simulation run. As main observables of our calculation, the particle yield and differential cross sections as emitted particle spectra and angular distribution at the end of the cascade phase of the spallation reaction are displayed.

Once determined the value of the free parameter of the model corresponding to the initial effective mass value,  $m_0^* = 0.9m_0$ , where  $m_0$  is the nucleon free mass value, in Fig. 4 we present the multiplicity of emitted nucleons at the end of the cascade phase as a function of the target nucleus atomic number, for the entire range of the incident beam energy studied. Solid, dashed, dotted, and dash-dotted lines stand for  $E_{\text{beam}} = 100, 150, 200,$  and  $250$  MeV, respectively. The behaviors for emitted protons and neutrons during the cascade are quite similar, as shown in Figs. 4(a) and 4(b). However, we observe an accentuated slope for the neutron yield corresponding to isospin asymmetry for heavier target nuclei. The separation between lines indicates that, for lower incident proton energy, the nucleon emission is still limited by the nuclear potential

well, demonstrating that nuclear effects are dominant for these energy ranges. Results for pion and neutron multiplicity are also displayed in Table III.

The greater value for proton yield as compared to neutron yield for low- $Z$  nuclei illustrates that, due to the nucleus transparency, the incident proton is emitted promptly after a few intranuclear collisions (sometimes right after the primary interaction). Another aspect of our calculation is the importance of peripheral interactions, i.e., for large impact parameter beam interactions with atomic nuclei, the emitted secondary particles number is incremented with respect to lighter, and more transparent, target nuclei.

The secondary proton spectra are shown in Figs. 5 and 6, displaying respectively results for  $p - A$  reactions with 100- and 250-MeV incident energy for  $p$ -C (solid lines),  $p$ -O (dashed lines),  $p$ -Ca (dotted lines),  $p$ -Se (dash-dotted lines), and  $p$ -Pb (dot-dot-dashed lines) reactions ( $m_0^* = 0.9m_0$ ). We have focused on this energy range because it comprises typical proton incident energy values attained in the specific themes stated earlier. A general behavior where the high energy of the spectra is enhanced for small values of the emitted particle angle is observed. This can be interpreted as the effect of peripheral interactions with the proton of the beam with

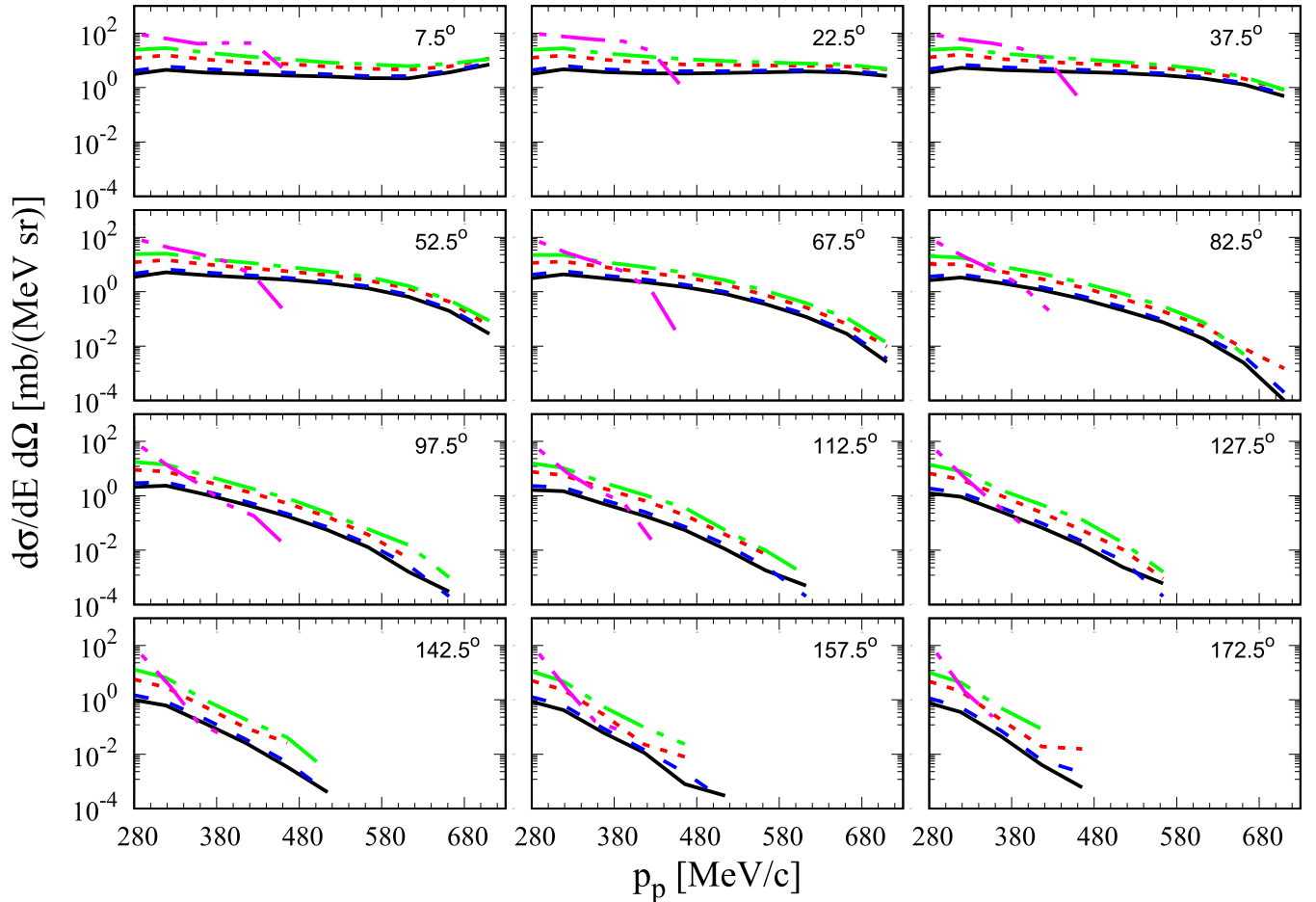


FIG. 6. Proton spectra for the  $p$ -A reaction with 250-MeV incident energy and emissions in different directions. Lines and panels are the same as those in Fig. 5.

nucleons of the target nucleus, delivering beam energy only partially as a ricochet effect or in a few interactions so that the emitted proton leaves the environment carrying most of the beam energy.

In this scenario, we can expect a tail in the distribution for large impact parameter interactions in which the incident proton suffers only a few (or just one) interaction, leaving the nuclear system with its initial kinetic energy value mostly unchanged. This effect is enhanced for low incident beam energy, where a slight slope of the spectra can be seen at frontal emitted proton angle values, mainly for the  $0 \leq \theta \leq 15^\circ$  window.

Another aspect observed from these figures is the degeneracy among the curves, in agreement with the particle yield shown in Fig. 4. The quasifree component of the present calculation allows us to infer that, once heavier target nuclei provide a larger number of emitted protons, larger values for the spectra will be obtained from these nuclei. This behavior is seen in all beam energy and proton emitted angle values. Also, although heavier target nuclei provide larger proton counts, the pattern of all curves are independent from the nucleus mass. This can be interpreted as, for transverse and even backward directions, the proton emission decreasing

for high momentum being mostly affected by a large number of intranuclear reactions of the incident proton delivering a large part of its energy to the nuclear environment.

In the present approach, we take into account both the Coulomb barrier and the nuclear surface to keep the target nucleus stable in its ground state. Thus, besides tunneling effects, to escape from the nuclear potential, any bound particles travels with kinetic energy high enough to classically overcome the potential well and restore its effective mass to the free nucleon mass value. Note that the potential well depth is adjusted to conform to the Fermi distribution (see Table II).

Because target nuclei employed in our study present isospin symmetry (light nuclei) and asymmetric (heavier nuclei), and once the beam is composed solely by protons, one can expect different behavior for protons and neutrons in terms of the energy of emitted particles in the frontal direction as the mass of the target nuclei increases. This can be noticed by comparing Figs. 5 and 6 with Figs. 7 and 8, respectively.

Similarly to Figs. 5 and 6, in Figs. 7 and 8 we display neutron spectra for  $p$ -Ca,  $p$ -O,  $p$ -Ca, and  $p$ -Se reactions. Results assert that heavier target nuclei again provide larger emitted neutron counts, as expected. However, differently from what

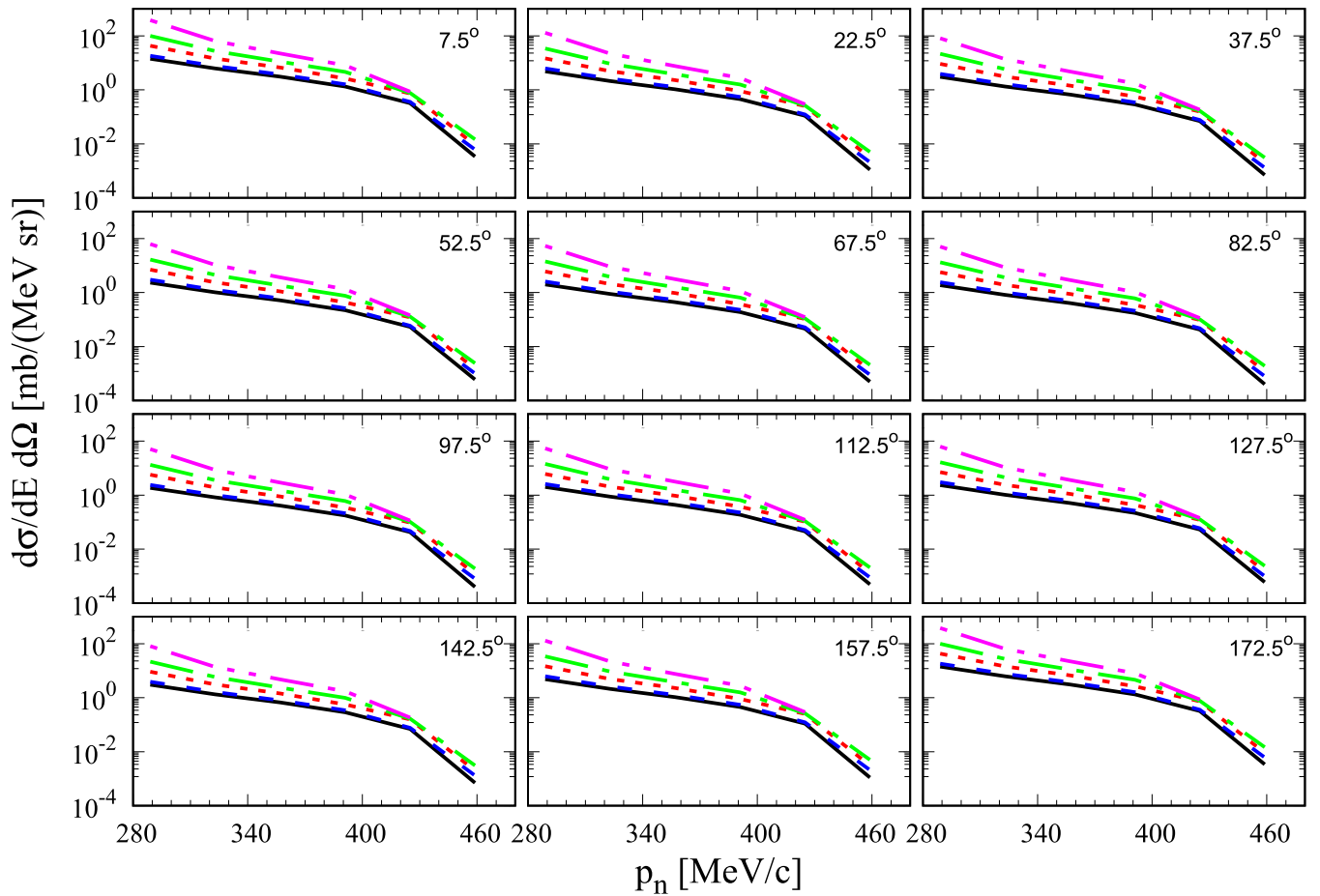


FIG. 7. Neutron spectra for the  $p$ -A reaction with 100-MeV incident energy. Lines and panels are the same as those in Fig. 5.

was observed for emitted protons, the behavior of emitted neutrons with respect to the momentum is less independent from the angle of the emitted neutron. Even so, it is possible to observe a small decrease in the neutron spectra for transversal angles (roughly a factor 2) with respect to the frontal and backward directions. This indicates that the first interaction of the proton of the beam with an environment neutron can cause its prompt emission instead of a sequence of several intranuclear interactions.

With respect to target nuclei, although the lines are very close in log scale, we observe a difference between the spectra for  $p$ -C and  $p$ -Se reactions by a factor near to 10. Again, this is a consequence of the increasing in the number of emitted neutrons by heavier nuclei. The difference among the curves decreases the more energetic the emitted neutrons become, highlighting that more energetic nucleons are emitted right after the primary interaction of the proton of the beam with the nucleons of the target nucleus.

From the overall aspect of all panels in Figs. 7 and 8, the idea that neutrons are emitted mainly after the nuclear thermalization is reached emerges, and also one shall expect that only a few neutrons are emitted right after the primary interaction. This idea could be important for practical issues where the precise determination of the energy or momentum distribution of secondary particles becomes a key ingredient for the determination of new quantities, such as absorbed dose

profile in tissue or energy delivery for secondary reactions in ADS.

Together with the particle spectrum, the angular distribution is another observable capable of elucidating the importance of nuclear effects on energy transference by proton beams to material in several applications. Thus, in Figs. 9 and 10 the emitted proton angular differential cross section is displayed for 100- and 250-MeV proton incident energies for the same target nuclei of earlier figures.

For low-energy emitted protons, we observe an almost isotropic proton distribution. However, as the energy increases, such as seen in Figs. 9 and 10 for  $E_p \geq 70$  MeV, a clear effect is that energetic protons come mainly from primary interactions. Transverse and backward directions are populated mostly by low-energy protons and, as a matter of fact, the slope of the curves is accentuated as the energy of the secondary emitted proton increases. In Fig. 9, for instance, there are only a few protons emitted, even for low scattering angles. One can also see that, as the emitted energy increases, the difference among target nuclei is hindered, evidencing once again that these emitted protons are mainly from the beam or those taken from the nuclear environment right after the primary interaction.

Concerning highly incident proton beams, a similar behavior is noticed, with the difference that the gross plateau one can see at 100-MeV incident energy is observed only

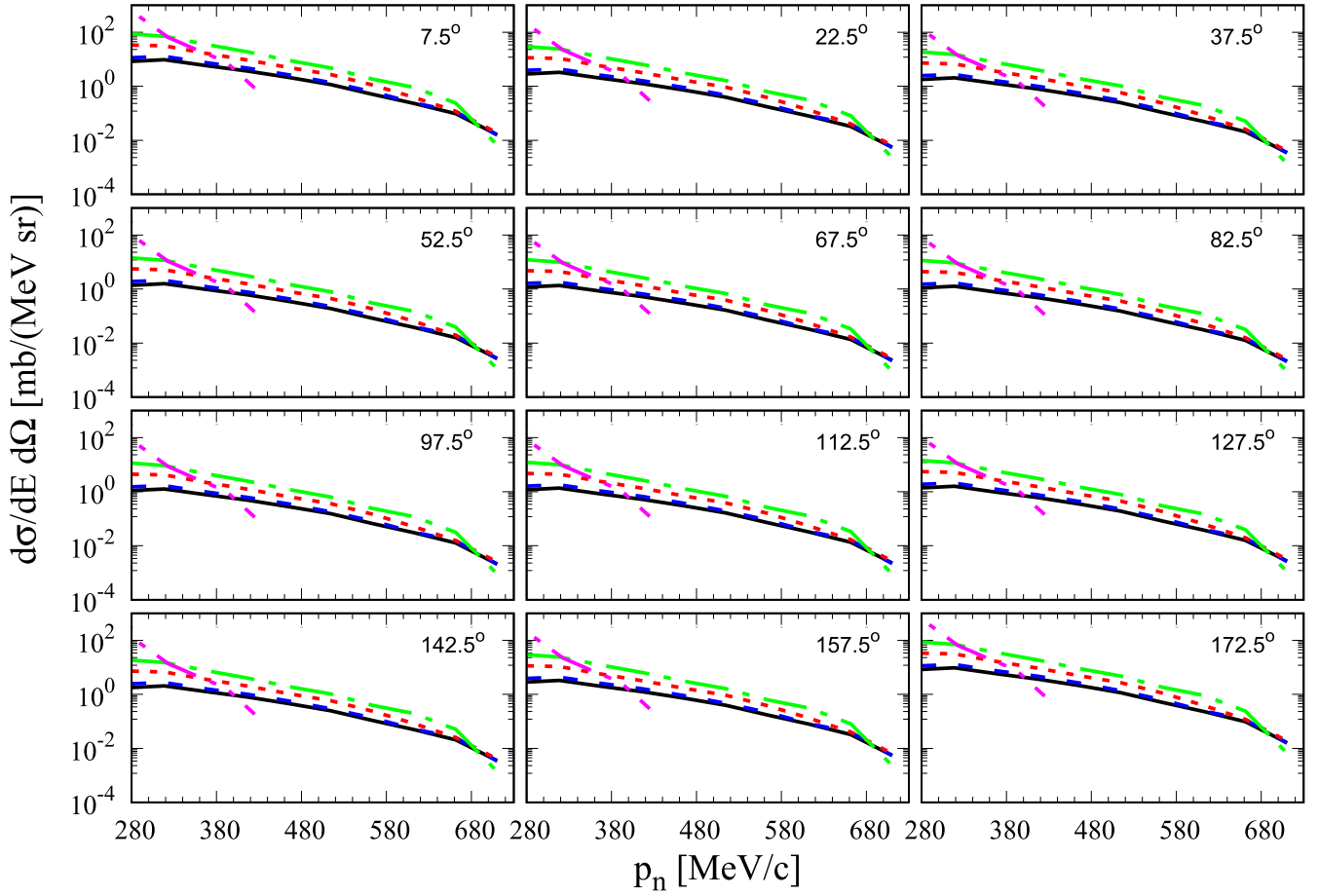


FIG. 8. Neutron spectra for the  $p$ -A reaction with 250-MeV incident energy. Lines and panels are the same as those in Fig. 5.

for very-low-energy emitted protons, i.e.,  $E_p \leq 50$  MeV. This behavior is expected since there is more energy delivered to the target nucleus, allowing the emission of more energetic protons at larger scattering angles. Once again, the curves are

practically superposed for the last panel, where particles with momentum near the proton beam momentum are detected.

The experimental nucleon-nucleon angular distribution is used to determine the kinematic final state of

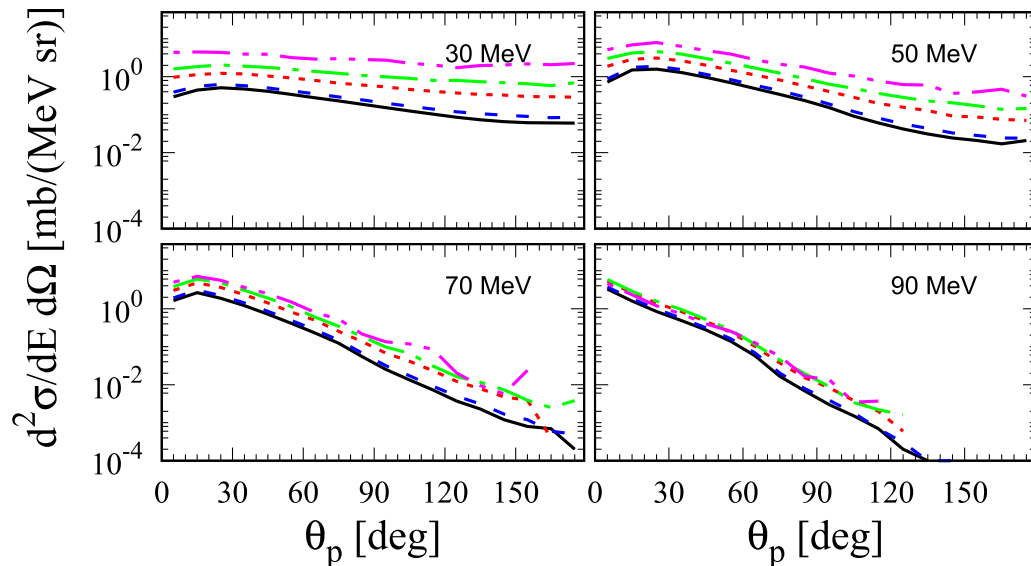


FIG. 9. Proton angular distribution for the  $p$ -A reaction with 100-MeV incident energy. Lines are the same as those in Fig. 5.



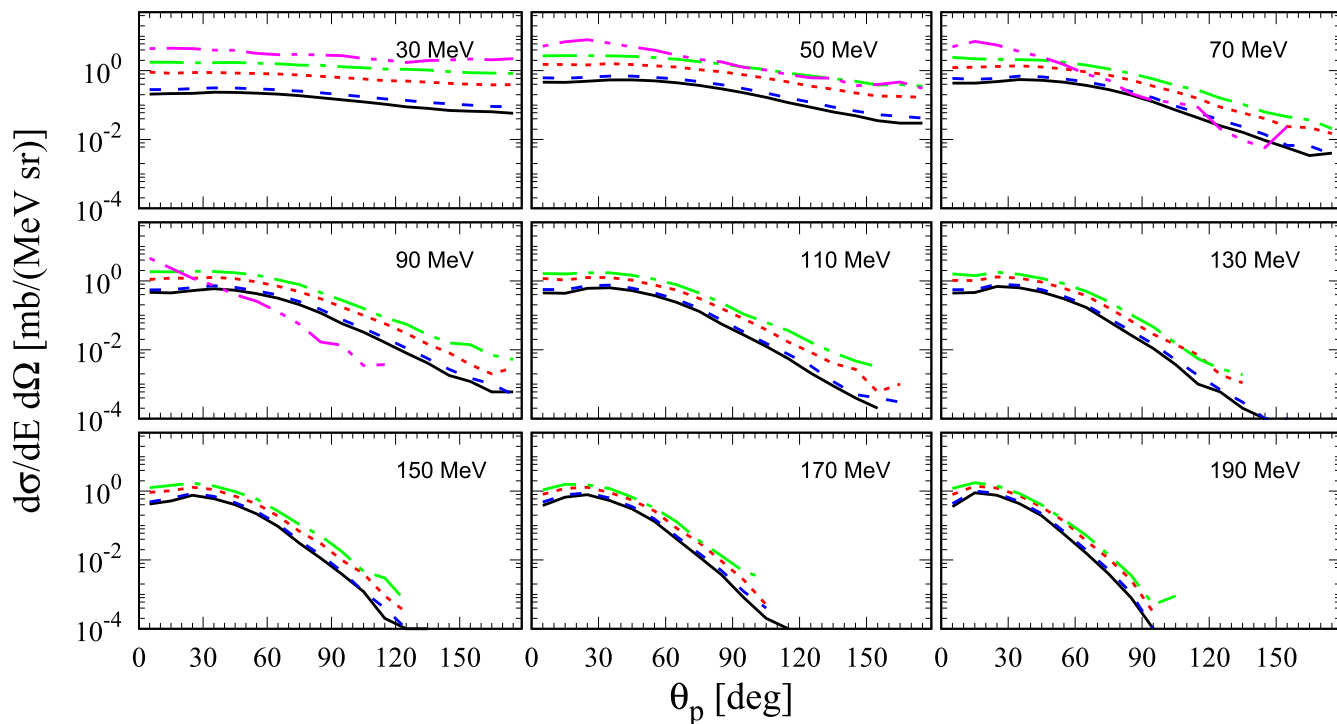


FIG. 10. Proton angular distribution for the  $p - A$  reaction with 250-MeV incident energy. Lines are the same as those in Fig. 5.

nucleons involved in the intranuclear collision. We remind that, for elastic collisions between similar mass particles, the scattering angle in the laboratory frame is one half of the center-of-mass scattering angle, which explains the roughly isotropic pattern for proton emission at low energies.

We stress that, although for light nuclei the angular distribution is roughly constant at low emitted energy values, as the nucleus mass number increases there is an indication that the angular distribution increases for larger angles. This is a clear consequence of the enhancement in the intranuclear

scattering interactions for high  $A$  values. Since the incident proton beam (and the nucleons from the target nucleus in the first interactions) interacts with a large ensemble of nucleons, central angles become favored in the distribution.

Angular distributions for secondary neutrons are displayed in Figs. 11 and 12 where lines are the same as those in Fig. 5. The behavior is quite similar to that observed for emitted protons' angular distributions, with the slight difference that, for low incident energy of the proton beam, i.e.,  $E_{\text{beam}} = 100$  MeV (Fig. 11), now the splitting in the curves

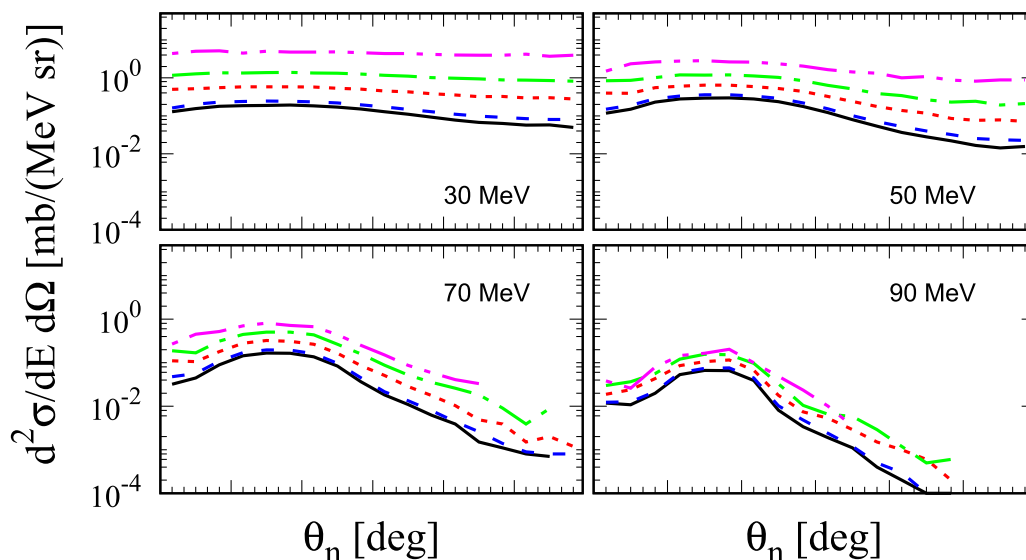


FIG. 11. Neutron angular distribution for the  $p - A$  reaction with 100-MeV incident energy. Lines are the same as those in Fig. 5.

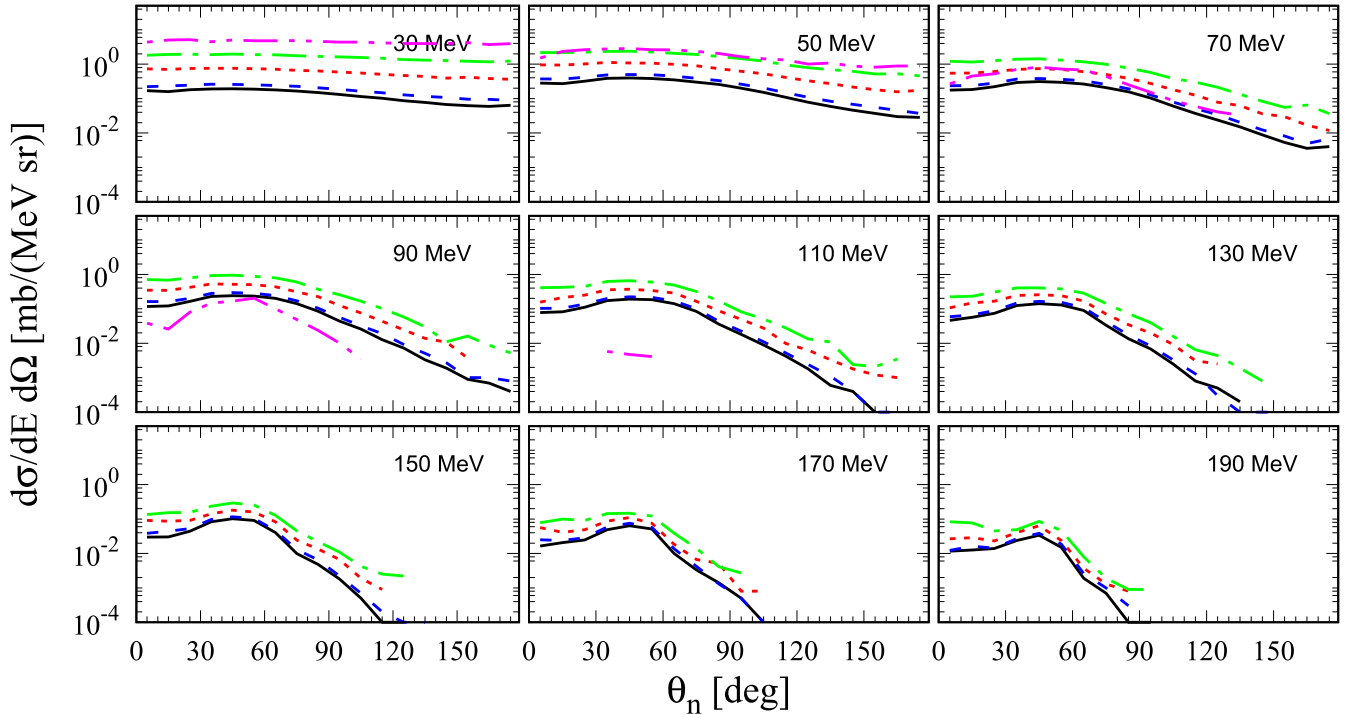


FIG. 12. Neutron angular distribution for the  $p - A$  reaction with 250-MeV incident energy. Lines are the same as those in Fig. 5.

for low energetic neutrons turns more relevant for larger target nucleus mass. Indeed, for  $E_n \leq 50$  MeV, the nuclear transparency slightly prevents larger angles' particle emission. This is finally seen as a thermalization effect of the nucleus because heavier nuclei provide a larger number of intranuclear interactions.

As the beam energy increases, the transparency effects become more significant for low-energetic emitted neutrons. In Fig. 12 this effect appears more significantly also for  $E_n < 90$  MeV. Indeed, as already discussed for emitted protons, highly energetic secondary neutrons populate the angular distribution mainly for frontal and, at most, transversal angles. We infer this behavior as a consequence of the primary interaction of the proton beam with neutrons from the target nucleus.

In the MCMC model, energy and momentum for nucleons from target nuclei are randomly set accordingly to a Fermi distribution. In all figures shown, for spectra and angular distributions we observe a decrease in the secondary particle population near the beam energy. This is a characteristic of spallation reactions, which should be dealt with in terms of a rapid phase, usually theoretically conceived as a cascade phase, and a slow phase, associated with the evaporation process. The results observed here point to an excited residual nucleus at the end of the cascade phase, which could produce low-energy secondary particles, known as evaporated particles, with energy lower than 20 MeV. These low-energetic secondary particles are very distinct from those from the cascade phase, so our results are clearly distinguishable and comparable to data.

Also, when aiming at practical issues such those cited earlier, the frontal dominance is increased with the target nucleus mass, leading to the conclusion that neutrons are preferably

emitted after the first initial interactions, far from the pre-equilibrium phase. Also, one can observe from the decrease in the neutron production at large angles that nuclear effects become significant, emphasizing that the nuclear energy content is strongly dependent on the nuclear field, here represented in terms of the nucleon effective mass.

In this section, we have presented several results for the most important observables in proton beam reactions at low incident energy: proton and neutron yield, spectra, and angular distributions. We regard these observables as key ingredients for the determination of secondary radiation propagation on material.

#### IV. CONCLUDING REMARKS

In the present work, we have determined the effects of the inclusion of an effective mass for bound baryons on yield, spectra, and angular distribution of these secondary particles. These effects highlight the relevance of nuclear contribution that could be useful for the determination of quantities of interest in practical issues such as dose profile calculation in proton therapy and energy delivered in ADS for nuclear waste recycling. Thus, we focus our attention on reactions with target nuclei that could produce results related to these issues.

Our results showed that a significant number of secondary particles are produced and scattered in different directions after proton beam interactions take place. However, the results showed that high-energy emitted nucleons are more frequent for frontal angles, i.e., they can be detected mainly in the beam direction. Also, we observed that peripheral reactions provide more energetic secondary particles and, consequently,

a higher-energy delivery in the frontal direction. Not less important, we also observed that, although with a smaller contribution, secondary particles in the backward direction can also be detected.

Thus, as a final conclusion, we presented a group of results for kinematic observables in spallation reactions asserting that secondary particles rise in a large number and contribute significantly to the energy of the momentum of the surrounding medium of target nuclei. We noticed that the scattered secondary particle emission from the beam interaction with the nuclear environment varies as a function of the baryonic effective mass, which mimics the effects of the nuclear mean field in the proton-nucleus reaction. We found  $m_0^* = 0.9m_0$  as the most suitable value for the initial ground-state effective mass value and we expect that this alternative for the nuclear effect mechanism could contribute somehow for new insights into the many-body interaction process. As the dynamics of the reaction take place, the effective mass value for all bound nucleons changes around this initial value.

A perspective of the present work is its extension to the problems mentioned above. A complete transport of this secondary radiation in the material should be more elucidating with respect to the total radiation transport in tis-

sue. Data provided with this new calculation could be applied to applications of proton beams such as the dose planned in commercial treatment planning systems. Then, we proposed that a detailed nuclear calculation becomes important in determining the total radiation transport to the material, a key ingredient in the investigation of the energy transferred and the absorbed dose delivered to material or tissue. The coupling of the present calculation to other Monte Carlo models (such as MCNPX or GEANT) is being studied and we aim to present results in future works.

## ACKNOWLEDGMENTS

We thank the support from the Brazilian National Nuclear Energy Commission (CNEN) for a postdoctoral fellowship, the Brazilian Coordination for Personnel Improvement (CAPES) for the research grant, and the Brazilian Council for Scientific and Technological Development (CNPq), for the technical support. Also, authors acknowledge the technological support of the Technology and Information Center NTI-UFAC and financial support of the National Institute of Science and Technology: Nuclear Physics and Applications - INCT-FNA.

- 
- [1] R. Serber, Nuclear reactions at high energies, *Phys. Rev.* **72**, 1114 (1947).
  - [2] P. R. O’connor and G. T. Seaborg, High energy spallation and fission products of uranium, *Phys. Rev.* **74**, 1189 (1948).
  - [3] A. Boudard, J. Cugnon, S. Leray, and C. Volant, Intranuclear cascade model for a comprehensive description of spallation reaction data, *Phys. Rev. C* **66**, 044615 (2002).
  - [4] M. Gonçalves, S. de Pina, D. A. Lima, W. Milomen, E. L. Medeiros, and S. B. Duarte, Many-body cascade calculation for photonuclear reactions, *Phys. Lett. B* **406**, 1 (1997).
  - [5] S. de Pina, E. de Oliveira, E. Medeiros, S. Duarte, and M. Gonçalves, Photonuclear  $K^+$  production calculation near threshold, *Phys. Lett. B* **434**, 1 (1998).
  - [6] J. Aichelin, “Quantum” molecular dynamics—a dynamical microscopic  $n$ -body approach to investigate fragment formation and the nuclear equation of state in heavy ion collisions, *Phys. Rep.* **202**, 233 (1991).
  - [7] V. E. Bunakov and G. V. Matvejev, The physical and mathematical foundations of the intranuclear cascade model algorithm, *Z. Phys. A* **322**, 511 (1985).
  - [8] J. Cugnon, A short introduction to spallation reactions, *Few-Body Syst.* **53**, 143 (2012).
  - [9] J. J. Griffin, Statistical Model of Intermediate Structure, *Phys. Rev. Lett.* **17**, 478 (1966).
  - [10] S. B. Jia, M. H. Hadizadeh, A. A. Mowlavi, and M. E. Loushab, Evaluation of energy deposition and secondary particle production in proton therapy of brain using a slab head phantom, *Rep. Pract. Oncol. Radiother.* **19**, 376 (2014).
  - [11] J. Pasternak, S. Schwenke, and J. Collot, Pion production at low energies, *Nucl. Instrum. Methods Phys. Res., Sect. A* **472**, 557 (2001).
  - [12] Y. Yamaguchi, T. Sanami, Y. Koba, and Y. Uozumi, Low-energy-threshold detector for measuring proton spectra at several tens of MeV using bragg curve spectroscopy, *Nucl. Instrum. Methods Phys. Res., Sect. A* **953**, 163158 (2020).
  - [13] J. F. Ziegler, M. Ziegler, and J. Biersack, Srim—The stopping and range of ions in matter (2010), *Nucl. Instrum. Methods Phys. Res., Sect. B* **268**, 1818 (2010).
  - [14] B. Santos, A. Pinheiro, M. Gonçalves, S. Duarte, and R. Cabral, On the nucleon effective mass role to the high energy proton spallation reactions, *Nucl. Phys. A* **948**, 78 (2016).
  - [15] J. W. Negele, The mean-field theory of nuclear structure and dynamics, *Rev. Mod. Phys.* **54**, 913 (1982).
  - [16] A. Boudard, J. Cugnon, J.-C. David, S. Leray, and D. Mancusi, New potentialities of the Liège intranuclear cascade model for reactions induced by nucleons and light charged particles, *Phys. Rev. C* **87**, 014606 (2013).
  - [17] T. Aoust and J. Cugnon, Effects of isospin and energy dependences of the nuclear mean field in spallation reactions, *Eur. Phys. J. A* **21**, 79 (2004).
  - [18] M. Jaminon and C. Mahaux, Effective masses in relativistic approaches to the nucleon-nucleus mean field, *Phys. Rev. C* **40**, 354 (1989).
  - [19] C. Mahaux and R. Sartor, Single-particle motion in nuclei, in *Advances in Nuclear Physics*, edited by J. W. Negele and E. Vogt (Springer, Berlin, 1991), Vol. 20, pp. 1–223.
  - [20] J.-C. David, Spallation reactions: A successful interplay between modeling and applications, *Eur. Phys. J. A* **51**, 68 (2015).
  - [21] D. Filges, S. Leray, Y. Yariv, A. Mengoni, A. Stanculescu, and G. Mank, in *Joint ICTP-IAEA Advanced Workshop on Model Codes for Spallation Reactions, (INDC(NDS)–0530)*, edited by G. Mank (International Atomic Energy Agency (IAEA), 2008).
  - [22] H. A. Abderrahim, T. Aoust, E. Malambu, V. Sobolev, K. Van Tichelen, D. De Bruyn, D. Maes, W. Haeck, and G. Van den Eynde, MYRRHA, a Pb–Bi experimental ADS: Specific approach to radiation protection aspects, *Radiat. Prot. Dosim.* **116**, 433 (2005).
  - [23] M. Blann, H. Gruppelaar, P. Nagel, and J. Rodens, International code comparison for intermediate energy nuclear data, *Nucl. Energy Agency-NEA* (1994), p. 206.

- [24] R. Michel and P. Nagel, International codes and model intercomparison for intermediate energy activation yields, Report No. NSC/DOC(97)-1, NEA/P&T No 14, OECD (Nucl. Energy Agency, Paris, 1997), [https://inis.iaea.org/collection/NCLCollectionStore/\\_Public/30/003/30003047.pdf](https://inis.iaea.org/collection/NCLCollectionStore/_Public/30/003/30003047.pdf).
- [25] G. Arduini, R. Cambria, C. Canzi, F. Gerardi, B. Gottschalk, R. Leone, L. Sangaletti, and M. Silari, Physical specifications of clinical proton beams from a synchrotron, *Med. Phys.* **23**, 939 (1996).
- [26] A. R. Smith, Proton therapy, *Phys. Med. Biol.* **51**, R491 (2006).
- [27] E. Medeiros, S. Duarte, and T. Kodama, The effect of nuclear binding energy on pion yields in relativistic nuclear collisions, *Phys. Lett. B* **203**, 205 (1988).
- [28] M. G. Gonçalves, E. L. Medeiros, and S. B. Duarte, Effect of multiparticle collisions on pion production in relativistic heavy ion reactions, *Phys. Rev. C* **55**, 2625 (1997).
- [29] I. L. Azhgirey, V. I. Belyakov-Bodin, I. I. Degtyarev, V. A. Sherstnev, S. G. Mashnik, F. X. Gallmeier, and W. Lu, CTOF measurements and Monte Carlo analyses of neutron spectra for the backward direction from a lead target irradiated with 200–1000 MeV protons, *Nucl. Instrum. Methods Phys. Res., Sect. B* **268**, 3426 (2010).
- [30] A. Deppman, O. A. de Paula Tavares, S. B. Duarte, E. C. de Oliveira, J. D. T. de Arruda Neto, S. Pina, V. P. Likhachev, O. Rodriguez, J. Mesa, and M. Gonçalves, The MCEF code for nuclear evaporation and fission calculations, *Comput. Phys. Commun.* **145**, 385 (2002).
- [31] J. Allison, K. Amako, J. Apostolakis, H. Araujo, P. A. Dubois, M. Asai, Barrand, R. Capra, S. Chauvie, R. Chytracek, G. A. P. Cirrone, G. Cooperman, G. Cosmo, G. Cuttone, G. G. Daquino, M. Donszelmann, M. Dressel, G. Folger, F. Foppiano, J. Generowicz *et al.*, Geant4 developments and applications, *IEEE Trans. Nucl. Sci.* **53**, 270 (2006).
- [32] A. Ferrari, P. R. Sala, A. Fassò, and J. Ranft, FLUKA: A multi-particle transport code (program version 2005), CERN Yellow Reports: Monographs (CERN, Geneva, 2005).
- [33] J. F. Briesmeister, Editor, MCNP—a general Monte Carlo *N*-particle transport code, version 4c, Technical Report, Los Alamos National Laboratory, Briesmeister, J. F. Editor (2000).
- [34] J. Blaizot and B. Friman, On the nucleon effective mass in nuclear matter, *Nucl. Phys. A* **372**, 69 (1981).
- [35] D. R. F. Cochran, P. N. Dean, P. A. M. Gram, E. A. Knapp, E. R. Martin, D. E. Nagle, R. B. Perkins, W. J. Shlaer, H. A. Thiessen, and E. D. Theriot, Production of charged pions by 730-MeV protons from hydrogen and selected nuclei, *Phys. Rev. D* **6**, 3085 (1972).
- [36] D. Carman, L. Bland, N. Chant, T. Gu, G. Huber, J. Huffman, A. Klyachko, B. Markham, P. Roos, P. Schwandt, and K. Solberg, Quasifree inclusive and exclusive cross sections at 200 MeV, *Phys. Lett. B* **452**, 8 (1999).